View Article Online
View Journal

RSC Applied Interfaces

Accepted Manuscript

This article can be cited before page numbers have been issued, to do this please use: A. P. Singh, B. Dutta and S. Chattopadhyay, *RSC Appl. Interfaces*, 2025, DOI: 10.1039/D5LF00261C.

ROYAL SOCIETY
OF CHEMISTRY

rsc.li/RSCApplInter

View Article Online
DOI: 10.1039/D5LF00261C

Received 00th January 20xx,
Accepted 00th January 20xx
DOI: 10.1039/x0xx00000x

Tin-oxide based binder-free light-weight nanostructured anode with high reversible capacity and cyclability for lithium-ion batteries manifesting the interfacial effect †

Adi Pratap Singh,†[a] Banadeep Dutta †[a] and Sudeshna Chattopadhyay *[a]

The advancement of lithium-ion batteries (LIBs) with higher storage capacity, energy density, and power density is critical to meet the growing power demands of modern technologies. Light-weight, micro-devices are attracting attention due to their growing demand in flexible and portable electronics, such as wearable health monitors, implanted medical devices, smart cards, and IoT sensors emphasizing the need for miniaturization of energy storage. This report describes a high-performance light-weight, binder-free tin-oxide (SnO_2) based nanostructured thin-film anode on copper (Cu) current collector for rechargeable LIBs, with lithium foil as counter electrode. Importantly, fabrication process of this binder-free electrode does not involve any kind of binders, conductive agents or any other additional inactive components (unlike the typical electrode preparation method), which results in providing improved energy density by reducing the effective weight of the LIB. Further it eliminates weak interaction and interface issues between binder and electrode material, thus minimizing active materials self-aggregation possibility, besides providing an increased accessibility of the electrolyte to the active material. The fabricated half-cell exhibits a significantly high reversible capacity of 1430 mAh g^{-1} and about 1200 mAh g^{-1} after 100 and 500 cycles respectively, at a current density of 0.3 A g^{-1} (0.2C), excellent cyclability, rate-performance (~800 mAh g^{-1} at 3 A g^{-1} at 110 cycles) and stability with a high coulombic efficiency (98-99%), as tested in the 0.02 to 1.8 V window. The activation of the electrode was achieved by controlled post deposition annealing process of optimized SnO_2 film on Cu, providing a suitable nanostructured hierarchical morphology and conformation involving SnO_2-Cu interface, which facilitates good electrical contact and enhanced electron/ion transport kinetics, yielding a high cyclability, rate performance and stability, preventing pulverization. Moreover, it brings forth an extra interfacial charge storage phenomenon via Cu/Li_2O nanocomposites, resembling capacitive characteristics. Stable capacity involving SnO_2 dealloying-alloying along with the interface induced extra lithium storage capability contribute to accomplish the observed high specific capacity of the electrode. This study provides an insight in designing of advanced light-weight electrode for next-generation energy-storage devices.

Introduction

As the global push for sustainable energy accelerates, the demand for efficient, scalable, and reliable energy storage systems (ESS) has surged. Driven by the rapid growth of renewable energy sources such as solar and wind, which are inherently intermittent, energy storage has become a critical component in ensuring a stable and resilient power supply.[1] Furthermore, the need for creative storage solutions to satisfy a variety of applications has increased due to developments in distributed energy systems, smart grids, and electric vehicles (EVs).[1-2] Batteries, being a class of energy storage, in general, play crucial role in ensuring an on-demand energy supply, holding equal importance to energy production. Modern needs emphasize the development of energy storage systems that are lightweight, flexible, environmentally friendly, and cost-effective with enhanced performance. Lithium-ion batteries (LIBs) have the highest energy density per unit volume or mass[3] and have been utilized to power a wide variety of electronic devices.[3-4] Intercalation-based lithium-ion batteries operate by inserting Li^+ ions into and extracting Li^+ ions from anode and cathode materials.[5] To obtain high energy density and a longer cycling life, it is critical to improve the reversibility of Li^+ insertion and extraction.[5] The production of lithium oxide (Li_2O) is a significant issue in oxide-based lithium-ion batteries. The formation of Li_2O results in high capacity, but Li^+ extraction from Li_2O is irreversible, as observed for oxide-based electrodes, resulting in limited reversibility in rechargeable Li-ion batteries.[6] When it comes to energy density, the working voltage (V) and specific capacity (mAh g^{-1}) of the electrodes, along with an appropriate operating potential window, are its primary determinants.[7] Moreover, in typical electrode fabrication, a pasted electrode is created on the current collector by combining active materials with a conductive additive and binder.[8] Because of the existence of the binders and other inactive components, issues like weak interaction and interface problem between binder and electrode material emerge, which causes self-aggregation of active materials and hence reduces the battery performance. Use of binder free electrodes not only minimize these issues but also show high electrolyte wettability.[9] Furthermore, binder-free thin film batteries offer the advantage of direct growth of active materials on the current collector thereby reducing the overall weight of the active electrode material and hence increasing the energy density of the active electrode[9] offering distinct advantages including long cycle life, and the ability to

[a.] *Department of Physics, Indian Institute of Technology Indore, Indore 453552, India. Email: sudeshna@iiti.ac.in, chattopadhyay.sudeshna@gmail.com.*
† Equal contribution and co-first authors.
†Electronic supplementary information (ESI) available: XPS and XRD results of A-SnO_2 electrode before and after 1st discharge, Attenuated total reflectance - Fourier transform infrared spectroscopy (ATR-FTIR) results, Comparison table for battery performance with A-SnO_2 and other thin-film electrodes, Quantification of the electrochemically active surface area (ECSA) of A-SnO_2 and B-SnO_2 electrodes from EIS data, Quantitative estimation of capacitive contribution to Li-ion charge storage for A-SnO_2 electrode, Photographs of A-SnO_2 and B-SnO_2 electrodes. See DOI: 10.1039/x0xx00000x

View Article Online
DOI: 10.1039/D5LF00266C

operate safely in a wide range of temperatures.[10] Additionally, their compatibility with flexible substrates and ease of integration into microdevices[11] make them ideal for next-generation applications. Sectors such as healthcare, where thin-film battery-powered advanced wearable biosensors and implantable medical devices, and electronics, where they enable slimmer and smarter gadgets, are driving demand for these cutting-edge solutions.[12] Despite these advantages, there are certain challenges/aspects in fabrication of binder-free electrodes, which include the compatibility of the electrode and current collector materials, which assures the proper adhesion capability (i.e., larger adhesion energy between the materials, in comparison to the cohesion energy of the deposited electrode material) to form a stable wetting thin-film electrode.[13] The adhesion between two materials depends on their relative surface energy, alternatively it relies on their relative dielectric polarizabilities.[13] Thus to grow an efficient binder-free thin-film batteries where active electrode material grow directly on a current collector, it is crucial to ensure excellent adhesion capability of the electrode material on current collector, hence a good electrical conductivity at the electrode-current collector interface. Substrate material/roughness induced mechanical interlocking of the deposited material also promote adhering ability.[14] [15] Furthermore, particular deposition technique, such as magnetron sputter deposition,[16] plays a role in this respect by yielding a favourable interface (even chemically rich), and hence a better adhesion.[16-17] Besides, the drive for eco-friendly and sustainable green-technology emphasizes the significance of binder-free thin-film batteries, employing safer materials, for superior recyclability, with reduced environmental impact.

Therefore, numerous efforts have been made to investigate novel high-capacity electrode materials in order to replace the standard graphite electrodes, which has a de-lithiation potential of approximately 0.3 V (vs. Li/Li^+)[18] and a low theoretical specific capacity of 372 mAh g^{-1}. Several materials have been studied as high-capacity anodes over the last two decades, including alloying-type metals like Sn, Al, Si, and Ge that can deliver capacities greater than 1000 mAh g^{-1} at potentials of ~0.5 V, and conversion-type transition metal oxides (MOx) like Co_3O_4, Fe_2O_3, and CuO that have capacities of ~800 mAh g^{-1} when de-lithiated at potentials > 2.0 V.[19] Among these, tin oxide (SnO_2) has garnered a lot of interest because of its high gravimetric capacities at moderate operating potentials.[20] The electrochemical lithiation of SnO_2 involves a conversion process ($SnO_2 + Li^+ \rightarrow Sn + Li_2O$) with a potential plateau of about 1.2 V and an alloying reaction ($Sn + xLi^+ \rightarrow Li_xSn$) at about 0.5 V.[21] These reactions correspond to the specific capacities of 711 and 783 mAh g^{-1}, respectively.[22] However, the following problems mostly prevent SnO_2 from reaching its full potential: (i) Occurrence of substantial volume changes during the intercalation and de-intercalation of Li^+ ions, causing issues of pulverization and detachment of active electrode material from the current collector, resulting in significant capacity degradation;[23] (ii) The low conductivity of SnO_2 at room temperature leads to a reduced electron transfer rate and sluggish reaction kinetics;[24] and (iii) Sn coarsening is another critical factor impacting capacity retention and contributing to the poor electrochemical performance of SnO_2.[25] This process promotes the agglomeration and growth of Li_2O particles or clusters, reducing electrical conductivity and hindering electron transfer to the inner Sn particles. As a result, the reversibility of the alloying and de-alloying reactions in Sn particles deteriorates.[25-26]

To overcome these issues different approaches involving implementation of varieties of nanostructured SnO_2 systems[22, 25, 27] along with the introduction of the suitable interfaces[28] have been reported in the literature.[22, 25, 27-29]

Nanostructured systems, in general, offering i) shorter Li^+ diffusion paths leading to faster reaction kinetics, ii) better volume expansion handling ability, iii) larger surface area that leads to more active sites for electrochemical reactions and iv) better electronic pathways thereby overcoming the low conductivity issues,[30] especially in metal oxides, play a huge role in improving the battery performance.[30-31] For SnO_2, the low conversion reaction reversibility and the pulverization problem, are the main issues for the degradation of the performance of the battery. However, nanostructured SnO_2 has the potential to partially overcome the conversion reaction reversibility issue due to the enhancement of the inter-diffusion kinetics among the Sn/Li_2O interface resulting from the shorter transfer distance of Li^+ and electrons.[3, 22, 25] On the other hand, nanocrystalline SnO_2 helps effectively in reducing the volume stress induced thus overcoming the pulverization problem.[29, 32] Subsequently, interface designing of SnO_2 nanostructured systems have also received attention as this engineered interface facilitates smooth lithiation/de-lithiation processes with faster Li^+ diffusion kinetics and creates hindrance to the Sn coarsening problem, which results in the enhancement of the lithium storage reaction reversibility.[28] In addition, excellent inherent adhesion capability of SnO_2 on conventional current collector (such as copper)[13, 33] enhances its potential as binder-free electrode material.

In this article, we report the development of high-performance binder-free tin-oxide (SnO_2) based thin-film electrode with copper (Cu) current collector, introducing the structural advantages at the Cu-SnO_2 interface, through controlled post-deposition heat treatment process. The thin Cu sheet acts as current collector and substrate for SnO_2 sputter deposition. The SnO_2 based electrode exhibits high specific capacity with stable capacity retention, for the half-cell tests with lithium (Li) sheet as counter electrode, for the rechargeable thin-film Li-ion batteries (LIBs) applications. We demonstrate that the post-deposition heat treatment induced designed hierarchical structure of the electrode involving SnO_2 thin film on Cu, introduce suitable interface, leading to significant enhancement in the effective conductivity of the system, providing improved charge transfer properties, suppressed pulverization issue in the SnO_2 active materials and activating extra interfacial charge storage capacity yielding overall enhanced energy density, rate performance, along with better stability and longer cycle-life, resulting in a high-performance electrode for rechargeable micro-battery systems.

View Article Online
DOI: 10.1039/D5LF00261C

Result and discussion

In this work, a new class of binder-free tin-oxide (SnO_2) based thin-film electrode with copper (Cu) current collector was investigated. Fig. 1(a) shows the The X-ray photoelectron spectroscopy (XPS) studies of the sputter deposited (RF) thin film (as detailed in the experimental section), signifying the formation of SnO_2, while Fig. 1(b) provides the tentative thickness of the deposited film, which was found to be about 60 nm, via cross-sectional field emission scanning electron microscopy (FESEM) images. Fig. 1a (i-iii) shows the XPS spectra of core Sn 3d and O 1s for the sputter deposited sample. Strong signals of Sn $3d_{5/2}$ and Sn $3d_{3/2}$ were present at 486.5 eV (Fig. 1a(i)) and 495 eV (Fig. 1a(ii)) respectively, whereas strong O 1s signal was there at 530.3 eV (Fig. 1a(iii)), which correspond to the formation of SnO_2 convincingly.[34] No signals corresponding to underneath Cu current collector were observed in the XPS spectra, indicating the high coverage pristine SnO_2 thin-film. Overall, the XPS and cross-sectional FESEM results in Fig. 1 signify the deposition of pristine SnO_2 thin-film of about 60 nm of thickness on Cu current collector via RF-sputtering. Further XPS study of the system after employing controlled post deposition heat treatment process, has been discussed later in the manuscript in context of electrochemical performance study of the electrode of interest, towards the explanation of the mechanism, and incorporated accordingly in **ESI†, Fig. S1†.**

Electrochemical studies

Galvanostatic discharge-charge (GCD):

The electrochemical performance of the LIB, comprised of SnO_2-based binder-free thin-film electrode (of thickness about 60 nm) with Cu current collector, and Li as counter electrode or anode, has been explored. Controlled heat treatment of magnetron sputter deposited SnO_2-thin-film on Cu current collector forge the electrode of interest here (assigned as A-SnO_2 electrode) for the rechargeable Li-ion battery (LIB) application, as demonstrated in Fig. 2. Fig. 2(a) shows the galvanostatic discharge-charge (GCD) profiles of the battery, cycled between 0.02 V to 1.8 V, at a current density of 0.3 A g^{-1} for different cycles. The specific voltage window (0.02 V to 1.8 V) has been selected to probe the specific capacity corresponding to SnO_2 system, involving alloying/de-alloying reaction at about 0.5 V. Cycle performance and Coulombic efficiency plot at current density of 0.3 A g^{-1} of the same are shown in Fig. 2(b). The system provides extremely high capacity in initial 15 cycles, which is more than 2000 mAh g^{-1}, with a sharp capacity fading with increasing cycle numbers, indicating an irreversible reactions /solid-electrolyte interphase (SEI) formation which occurred in this voltage window. It starts getting stable from 35 cycles onwards, i.e., 1700 mAh g^{-1} at 35 cycles, which reaches to 1430 mAh g^{-1} at 110 cycles, and a reasonably stable capacity afterward. Specific capacity remains steady at around 1200 mAh g^{-1} from 250 cycle to 500 cycle, and onwards. This result imply

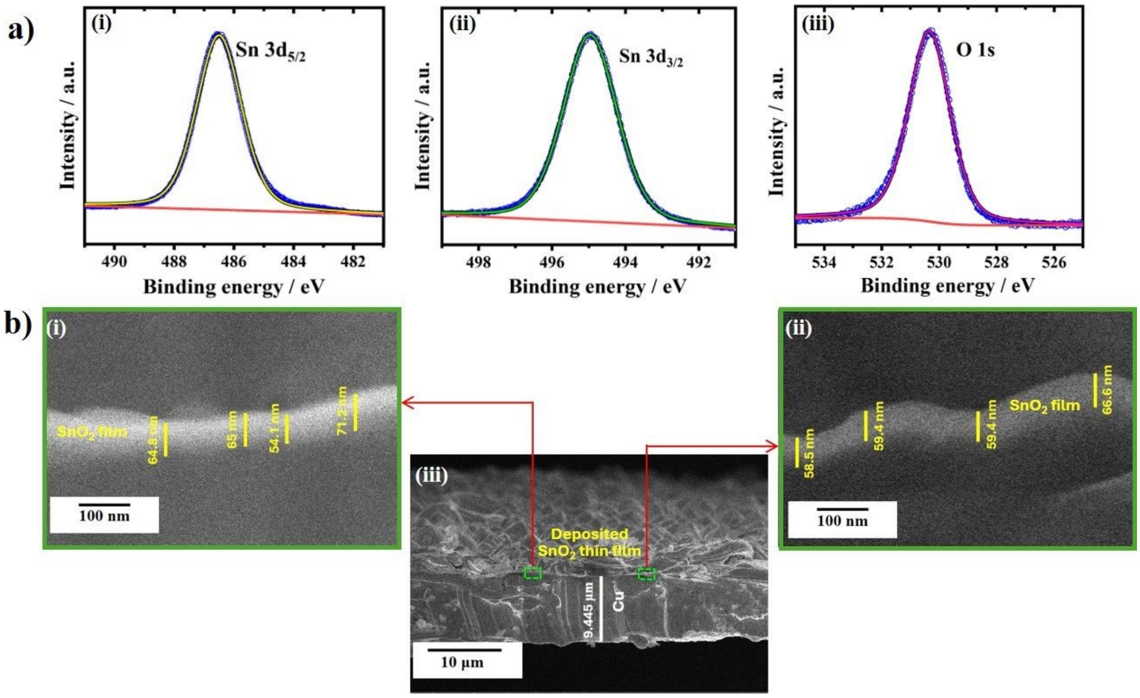

Fig. 1 Pristine SnO_2 thin film (RF-magnetron sputter deposited) on Cu current collector. (a) XPS spectra of Sn $3d_{5/2}$ (i), Sn $3d_{3/2}$ (ii) and O 1s (iii), signifying the deposited SnO_2 film. (b) Cross-sectional FESEM images at two different magnifications with respective scale bars; two magnified images (i)-(ii), indicating thickness of the deposited SnO_2 thin film, along with the overall cross-sectional image of the RF sputter deposited SnO_2 thin film on Cu current collector (iii).

View Article Online
DOI: 10.1039/D5LF00261C

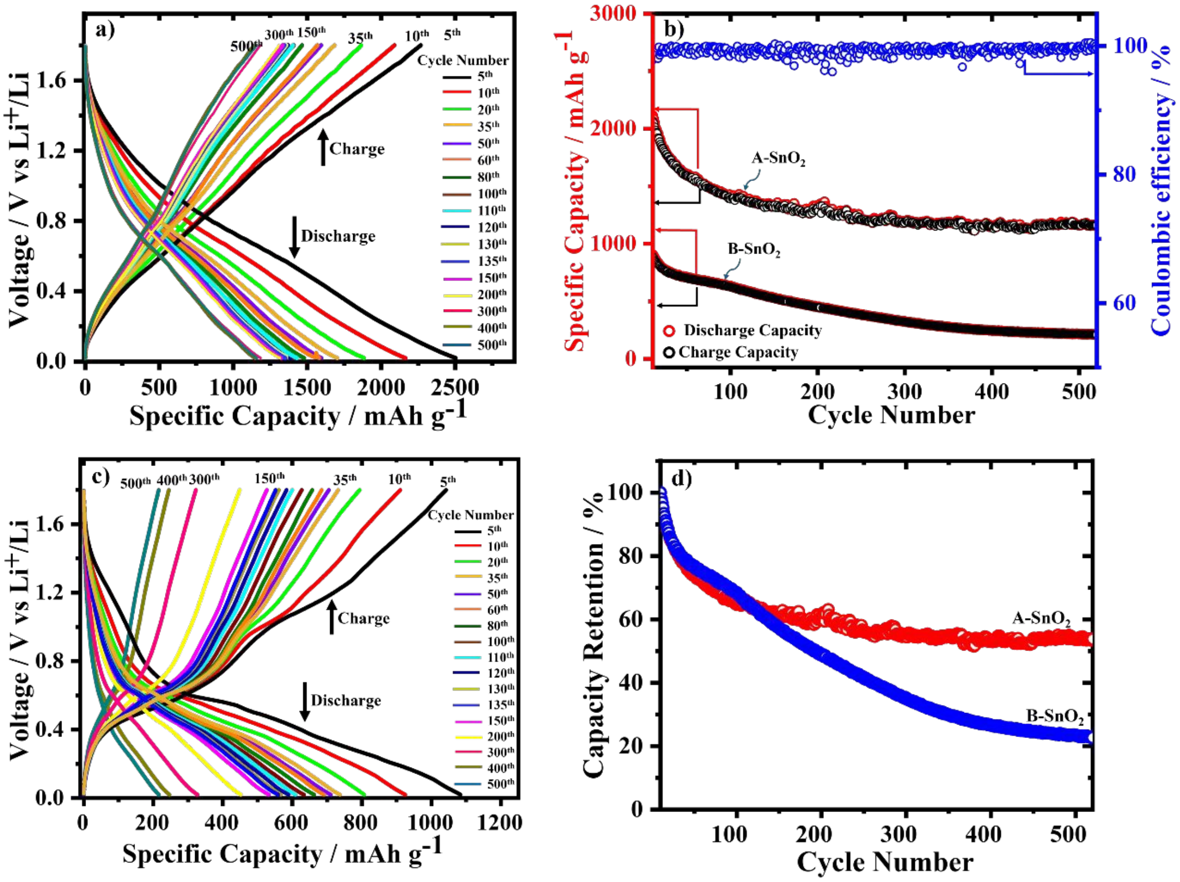

Fig. 2 Electrochemical characterization of electrodes A-SnO_2 and B-SnO_2. (a) Galvanostatic charge/discharge profiles of A-SnO_2 electrode at a current density of 0.3 A g^{-1} for different cycles. (b) Cycle performances (from 10th to 520th cycle) of both the electrodes along with the coulombic efficiency plot of A-SnO_2 electrode, at a current density of 0.3 A g^{-1}. (c) Galvanostatic charge/discharge profiles of B-SnO_2 electrode at a current density of 0.3 A g^{-1} for different cycles. (d) Capacity retention (from 10th to 520th cycle) of A-SnO_2 and B-SnO_2 electrode.

that the post deposited heat treated SnO_2 thin film on Cu current collector delivers higher specific capacity in comparison to that of the experimental results reported in the literature involving various SnO_2 based electrodes (which was found to have a maximum of about 800 mAh g^{-1}).[3, 22, 25, 27, 29] Secondly, the observed stable capacity, 1200 mAh g^{-1} (at higher cycles, >250-cycle) is greater than the theoretical capacity of alloying/dealloying reaction solely (i.e., 783 mAh g^{-1}), signifying the activation of some other reactions or influences based on the interfacial effects in the SnO_2 nanostructured electrode system, which will be discussed and explained in the following section, in connection with the cyclic voltametric (CV) response of the system. A high Coulombic efficiency (□ 98-99%) is evident for this system (Fig. 2(b)). Furthermore, the electrode exhibits a remarkably high stability and long cycle life (Fig. 2(a), (b), and (d)), as compared to the other available/reported SnO_2 based electrodes, [3, 22, 25, 27, 29, 35] and hence reveals a remarkably high performance of the system. The observed electrochemical performance of A-SnO_2 is also superior as compared to the other available/reported thin-film electrodes, including other tin-oxide based electrodes, [3, 22, 35-36] when used in equivalent micro battery systems, [3,22, 25, 27, 35-37] relevant comprehensive information is shown in Table S1†.

A comparison study using equivalent untreated SnO_2 thin film electrode on Cu current collector was carried out, as presented in Fig. 1(b-d). Growth parameters for RF-sputter deposited SnO_2 were kept same for both the electrode systems (as discussed in the experimental section). Optimization of the growth parameters were carried out to achieve a high-quality film to avail better performance of the electrode.

For convenience, in this report now onwards, before and after post deposition heat treated SnO_2 thin film on Cu current collector systems have been referred respectively as untreated SnO_2 electrode ("B-SnO_2") and electrode of interest ("A-SnO_2").

Both the treated and untreated SnO_2 electrodes (A- SnO_2 and B-SnO_2) exhibit an initial high capacity with a sharp falling trend in the first few cycles as shown in Fig. 2 (b) and (d), which can be attributed to the irreversible reactions or solid-electrolyte interphase (SEI) formation, and can be ascribed to the occurrence of irreversible conversion reaction in SnO_2, ($SnO_2 + 4Li^+ + 4e^- \rightarrow Sn + 2Li_2O$), which corresponds to theoretical capacity of about 711 mAh g^{-1}.[22, 25, 38]

The untreated SnO_2 (B-SnO_2) electrode shows a low specific capacity of about 700 mAh g^{-1} at 100-cycle, which is 50% lowered in comparison to that of the post deposition heat treated SnO_2 electrode (A-SnO_2) at same cycle. However, after exhibiting some sort of stability for ~35-100 cycle window, B-SnO_2 reveals a sharp fall in specific capacity with increasing electrochemical cycle number, which leads to ~216 mAh g^{-1} capacity at 500-cycle, which was even lower, and only 18% of the capacity of A-SnO_2 at same cycle, as displayed in Fig. 2(c). The observed capacity of about 700 mAh g^{-1} up to 100-cycle for B-SnO_2 was in consistence with the reported experimental results for the other SnO_2 based electrodes in the literature,[25, 27, 38] and can be attributed to the contribution from reversible alloying/de-alloying reaction ($Sn + xLi^{+} + xe^{-} \leftrightarrow Li_xSn$) of SnO_2.[22, 25, 38] Here, the 'x' in the alloying/de-alloying reaction signifies the number of Li atoms containing in the Li-Sn alloy, per metal (here Sn) atom. The ratio of the number of Li atoms to the number of metal atoms must be as high as possible to enhance the capacity of the working electrode.[38] Theoretically, for x=4.4, maximum Sn lithiated phase $Li_{22}Sn_5$ is obtained which corresponds to a specific capacity of 783 mAh g^{-1}.

At 500 cycles, the capacity retention for B-SnO_2 is of around 22% (and 29%) with respect to its initial 10th cycle (and the 35^{th} cycle), as displayed in Fig. 2(d). Such phenomenon can be ascribed to the commonly observed pulverization issues associated with the SnO_2 based electrodes, [39] leading to a sharp capacity loss, compromising the stability of the electrode, and thus performance of the overall battery. The low conductivity of SnO_2 is also one of the reasons for the pulverization problem. The observed electrochemical performance of B-SnO_2 is consistent with the reported literature involving the SnO_2 film based electrodes.[25, 39-40] In this regard, it should be noted that most of the published report with general SnO_2 based electrode in LIB, presented the specific capacity only up to 100-200 cycles.[3, 25, 39-40]

Such a large capacity fading after ~100 cycles was mostly overcome in post deposition treated SnO_2 electrode (A-SnO_2), as shown in Fig. 2(a), (b), and (d). A higher capacity retention of 56% (and 71%), with respect to its initial 10^{th} cycle (and the 35^{th} cycle), was evident for A-SnO_2, as shown in Fig. 2(d), implying a better conductivity, lesser Sn-coarsening effect in the system and reduced pulverization issue.

The rate performance of A-SnO_2 at the current densities from 0.3 A g^{-1} (0.2C) to 3 A g^{-1} (2C) was studied, as shown in Fig. 3. Even at the high current densities (high rates) of 0.9 A g^{-1} (0.6C), 1.5 A g^{-1} (1C) and 3 A g^{-1} (2C), competitive discharge capacities of A-SnO_2 of ~1340 mAh g^{-1}, ~1100 mAh g^{-1} and ~800 mAh g^{-1} at 50, 60 and 110 cycles were maintained respectively (blue open-circle plot, Fig. 3). Moreover, reversible capacity of ~1150 mAh g^{-1} and ~1350 mAh g^{-1} could be recovered after 120 and 150 cycles upon reducing the current to 0.9 A g^{-1} (0.6C) and 0.3 A g^{-1} (0.2C). For reference the A-SnO_2 specific capacity at a constant current density, 0.3 A g^{-1} (0.2C), is presented (red solid-circle plot) along with that of the varying current density plot (blue open-circle), in Fig 3. The results manifest a remarkable

View Article Online
DOI: 10.1039/D5LF00261C

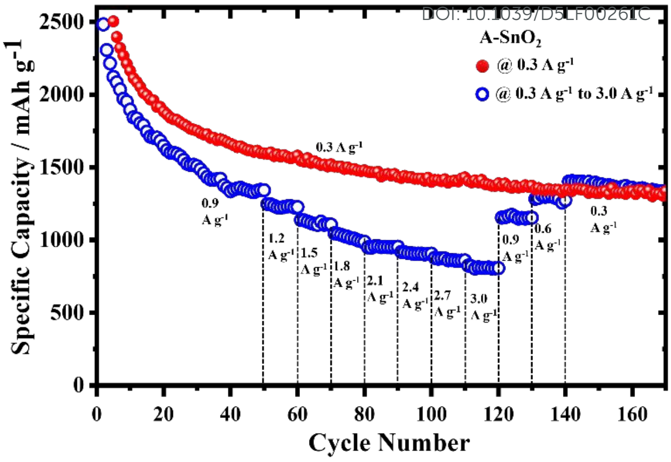

Fig. 3 Rate performance of A-SnO_2 at different current density (rate) from 0.3 A g^{-1} (0.2C) to 3 A g^{-1} (2C).

rate-performance of the A-SnO_2 electrode, signifying the preserved specific capacity even after the repetitive cycles at relatively high rates.

The explanation for such superior performance of A-SnO_2 has been explored through study of cyclic voltametric response (CV), electrochemical impedance spectroscopy (EIS), FESEM and UV-Vis spectroscopy.

Cyclic voltametric response (CV):

A typical CV scan of A-SnO_2 electrode (with $LiPF_6$ electrolyte and metallic lithium as counter electrode, a similar assembly as GCD measurement) in the voltage window 0.05 to 1.8 V, focusing the potential region of lithium alloying-dealloying reaction,[41] at a slow scan rate of 0.05 mV sec^{-1} is shown in Fig. 4(a). While the CV scan of B-SnO_2 with same scan parameters is displayed in Fig. 4(b) for the comparison purpose with same x-y scale. It can be seen that there are two pairs of redox peaks which appeared at the CV scan of A-SnO_2 corresponding to predominantly two Li-Sn alloying and dealloying reactions, forming $Li_{22}Sn_5$ (0.18 V, 0.47 V) and LiSn (0.56 V, 0.76 V) phases, [41-42] depicted as (E_{R1}, E_{O1}) (E_{R2}, E_{O2}) in Fig. 4(a). When these results are compared with that of B-SnO_2, it clearly shows that the Li-Sn alloying reaction, E_{R1}, corresponding to $Li_{22}Sn_5$ (0.18 V), shifts rapidly towards lower lithium contained phase with increasing scan number, and saturates at about Li_7Sn_3 (0.4 V) phase, [41-42] by 15 cycles, as depicted in Fig. 4(b). While the second redox reaction (E_{R2}, E_{O2}) corresponds to alloying with lowest lithium contain LiSn phase, exhibiting similar voltages as that of A-SnO_2.

Furthermore, Fig. 4 clearly shows the considerable enhancement in the area of the cyclic voltammogram of A-SnO_2 in comparison to B-SnO_2, implying the distinctively higher charge accumulation capacity or higher specific capacity[43] for A-SnO_2 electrode, which is consistent with the GCD results, discussed in the previous section. It is evident

DOI: 10.1039/D5LF00261C

that the enhancement in the specific capacity predominantly relies on the emergence of significant capacitive behaviour in A-SnO_2 electrode. To investigate the origin of such capacitive behaviour, the first cathodic scan (Fig. 4(c-d) is examined carefully. In the first nanocomposites, (or Me/Li_2O nanocomposites where Me represents the transition metals that do not alloy with Li) are responsible for an extra Li storage at low potential for rechargeable Li batteries,[45] and contribute as interfacial charge storage resembling the characteristic

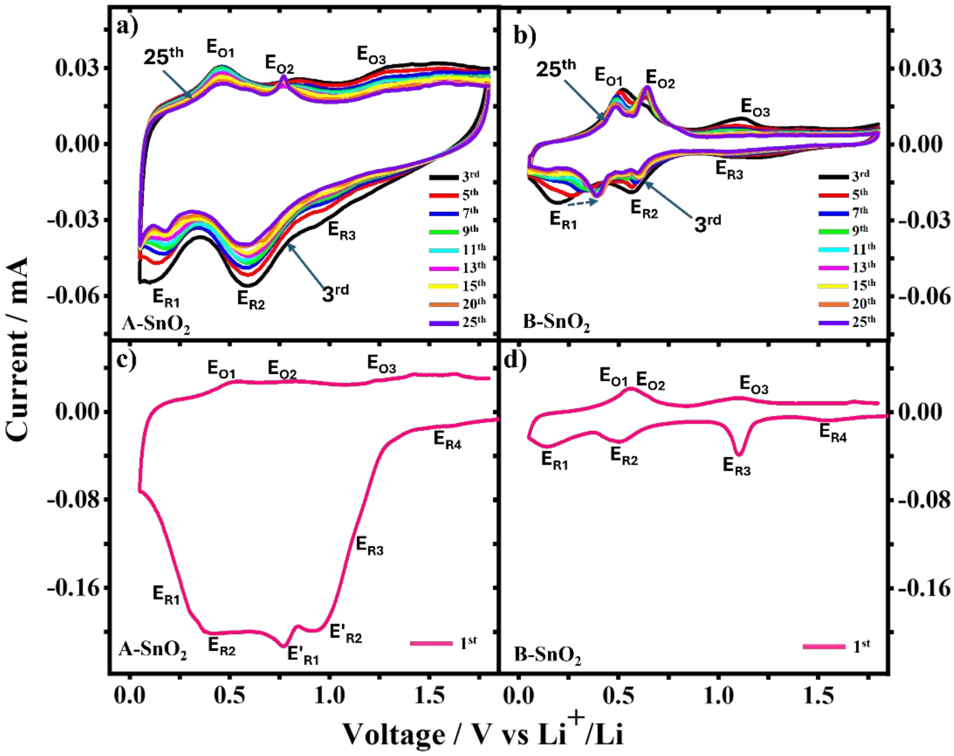

Fig. 4 Cyclic Voltammogram (CV) of electrodes (a) A-SnO_2 and (b) B-SnO_2, for the 3rd, 5th, 7th, 9th, 11th, 13th, 15th, 20th, and 25th cycles at a scan rate of 0.05 mV sec^{-1}. CV of the electrodes, (c) A-SnO_2 and (d) B-SnO_2, for the 1st cycle at the same scan rate of 0.05 mV sec^{-1}.

cathodic scan of B-SnO_2, there are a weak broad reduction band and an intense sharp band at 1.5 V and 1.1 V respectively, which are ascribed to the two-step irreversible conversion reaction of SnO_2 ($SnO_2 + 4Li^+ + 4e^- \rightarrow Sn + 2Li_2O$),[22, 28] depicted as E_{R4} and E_{R3} respectively in Fig. 4 (d). However, in the first cathodic scan of A-SnO_2 (Fig. 3(c)), apart from a weak signal from E_{R4} at ~1.5 V, a broad intense reduction band appeared in the range of about 0.7-1.1 V. The broad intense band includes $E_{R3,}$ and predominantly represent the intense two step conversion reactions involving CuO to produce Cu and Li_2O ($CuO + 2Li^+ + 2e^- \leftrightarrow 2Cu_2O + Li_2O$; $Cu_2O + 2Li^+ + 2e^- \leftrightarrow 2Cu + Li_2O$) at 1.06 V ($E'_{R2}$) and 0.79 V ($E'_{R1}$) respectively,[44] which do not prevail in the reversed anodic scan (as the corresponding oxidation reactions from Cu to CuO take place at above 2.4 V, which is beyond the set volage window, 0.05-1.8V, focused on the lithium alloying-dealloying reactions), and disappeared thereafter in the higher cycle cathodic scans. Formation of CuO in A-SnO_2 system, and its reduction producing Li_2O after first discharge were also evident in ex-situ XPS results as shown in ESI†, Fig. S1†. While, the Cu current collector enacts the formation of CuO, in consequence of the controlled post deposition heat treatment of A-SnO_2. Essentially, such Cu/Li_2O of a capacitor, as established and reported in the literature.[45-46] Quantitative capacitive contribution[47] was estimated, which was found to be of about 39%, as shown and described in ESI†, Fig. S2†. In this regard, the differences in voltage profiles between samples, A-SnO_2 and B-SnO_2, (Fig. 2(a) vs. 2(c)), as observed from GCD study, signifying an additional capacitive contribution to the specific capacity of A-SnO_2 (Fig. 2(a)), obscuring the prominent plateaus as observed in B-SnO_2 (Fig. 2(c)), e.g., plateaus at 0.56 V and 0.47 V in discharge and charge profiles respectively) corresponding Li alloying dealloying reactions, further supports the above inference revealing the extra Li storage through capacitive characteristic.

Hence, the origin of such observed higher stable capacity in A-SnO_2 electrode relies on the formation of Cu/Li_2O nanocomposites, which plays role to enhance the specific capacity effectively through interfacial charge storage mechanism via capacitive behaviour.[45] Surface morphology study and UV-Vis results, as presented in the next sections, support the inference consistently.

Overall, the results from CV are consistent with that of GCD. The CV results shows that the peak voltages are nearly similar thereby maintaining a constant electrochemical stability of the cathode after 15 cycles, which well supports the GCD results and the cycle performance plots.

Electrochemical impedance spectroscopy (EIS):

Electrochemical impedance spectroscopy (EIS) spectra were collected on the cells with A-SnO_2 and B-SnO_2 electrodes, after formation (Fig. 5(a)) and cycling (Fig. 5(b)), and were fitted using the equivalent circuit model (as shown in the insets),[48] involving R_s, R_{ct}, CPE_{dl} and CPE_w. Where, R_s, R_{ct} and CPE_{dl} correspond to the solution resistance (from the electrolyte), the charge transfer resistance and constant phase elements representing the double layer capacitance respectively. [48-49] Whereas, constant phase element, CPE_w, represent the Li-ion diffusion related behaviour of the cell which conglomerates Li diffusion process taking place at electrode.[48-50] CPE_{SEI} and R_{SEI} (in Fig. 5(b)) represent constant phase element related to non-ideal capacitance of SEI layer and resistance for Li-ion diffusion in the SEI layer respectively, which emerge during the cycling.[49, 51] Fig. 5 shows that the charge transfer resistance (R_{ct}) of

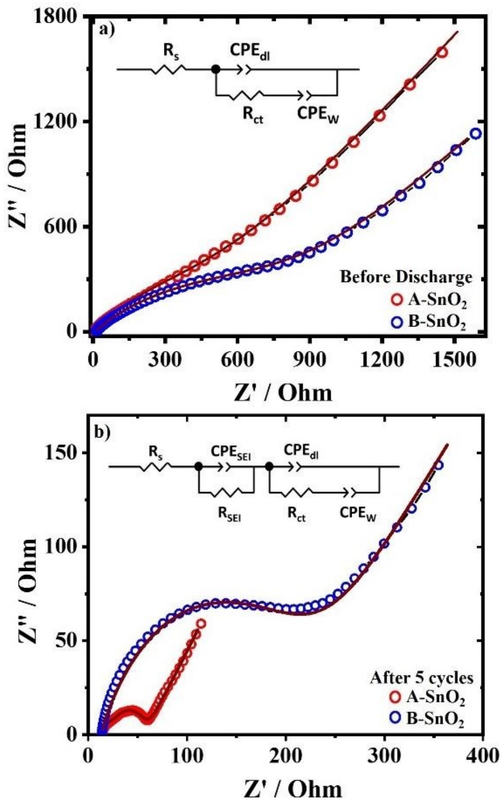

Fig. 5 Electrochemical impedance spectroscopy (EIS) data of A-SnO_2 (red open-circle) and B-SnO_2 (blue open-circle) electrodes before (a) and after (b) cycling, along with the corresponding fitting lines (solid-brown lines) using respective equivalent circuit models as shown in the respective insets.

the cell with A-SnO_2 electrode is lesser in comparison to that of B-SnO_2, where the difference became more prominent after a few numbers of cycling the cells, as evident for Fig. 5 (a) and (b). As per the general convention, charge transfer resistance (R_{ct}) was estimated considering the EIS plot of cycled electrode (for a few cycles)[49, 52] which corresponds to Fig. 5(b). After cycling the batteries for few cycles (5 cycles), the R_{ct} values for A-SnO_2 and B-SnO_2 were found to be of about ~34 Ω and ~212 Ω respectively (Fig. 5(b)). The results (Fig. 5(b)) indicate about 84% reduction in charge transfer resistance in case of A-SnO_2 system, the electrode of interest, in comparison to B-SnO_2, the untreated one. (EIS data collected prior to the battery cycling show the R_{ct} values of about 980 Ω and 1093 Ω respectively for A-SnO_2 and B-SnO_2 (Fig. 5(a)). These findings indicate much less resistive interfaces formed by the A-SnO_2 over B-SnO_2 thereby contributing to the improved electrochemical performance which supports the observed superior cycle performance via GCD profiles.

Morphology:

The morphological information of the developed binder free thin film SnO_2 based electrodes was obtained by Field Emission Scanning Electron Microscopy (FESEM) and displayed in Fig. 6.

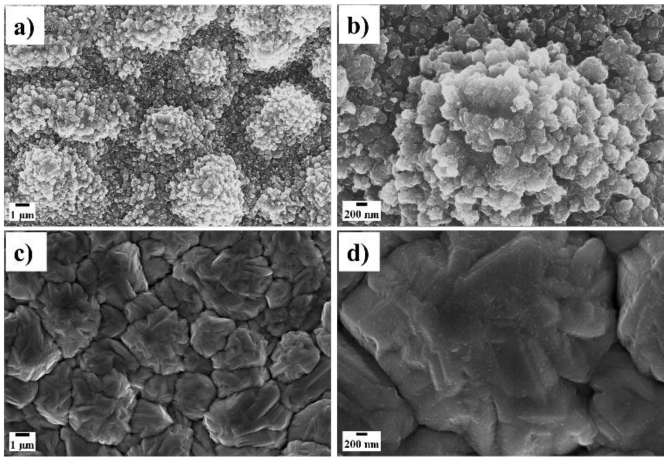

Fig. 6 FESEM images of A-SnO_2 ((a), (b)) and B-SnO_2 ((c) and (d)) electrodes in two different magnifications along with respective scale bars.

Fig. 6 (a-b) show two different magnifications of FESEM images of post deposition heat treated binder-free A-SnO_2 electrode exhibiting a nano-structured flower with nano-petals like morphology all over the electrode, leading to a large surface area, availing the potential to deliver improved charge transfer capability by providing a proper channel for the ions in their transportation.[53] On the other hand, abundance of nano-crystallites in the electrode morphology, also helps effectively in reduction of the induced volume stress, thus minimize the pulverization issue.[30] Fig. 6 (c-d) display the FESEM images of corresponding untreated electrode, B-SnO_2, with equivalent magnifications, for comparison purpose. It is evident that the A-SnO_2 electrode, possessing regularly arranged nanostructured subunits with large number of nano-voids and high specific area void borders that facilitates the lithiation/de-lithiation process, shortens the Li^+ transfer distances and creates hindrance to the Sn coarsening, resulting in the enhancement of lithium storage, and reaction reversibility. Furthermore, the larger electrochemical surface area (ECSA)[54] of A-SnO_2 as compared to B-SnO_2 was also verified quantitively through EIS study, as described in ESI†, S2†. Thus, this improved morphology facilitating smooth ion transportation within the A-SnO_2 electrode, significantly contributed to a remarkable rate performance of the system also, as evident in Fig. 3.

The results signify that the constituents, structure, conformation and advantageous morphology of A-SnO_2 provide a pathway for high interfacial charge storage capacity along with higher amount of Li intercalation in the system, which activated the overall system efficiently, thereby showing an improved electrochemical performance.

UV-Vis study:

The electronic properties, specifically the effective band edge or band gap of A-SnO_2 system was examined in comparison to B-SnO_2 via UV-Vis spectroscopy in diffuse reflectance mode (DRS), as displayed in Fig. 7. The plot of $(F(R)\ h\upsilon)^2$ versus photon energy $h\upsilon$ is shown in Fig. 7, where $F(R)$ is the Kubelka–Munk function,[55] as represented in equation 1, and R is the diffuse reflectance. The extrapolated line at $(F(R)\ h\upsilon)^2 = 0$ gives the tentative value of the band gap in eV,[56] $F(R)$ is proportional to the absorption coefficient, and expressed as,[57]

$$F(R) = \frac{(1-R)^2}{2R} \qquad \text{-- (1)}$$

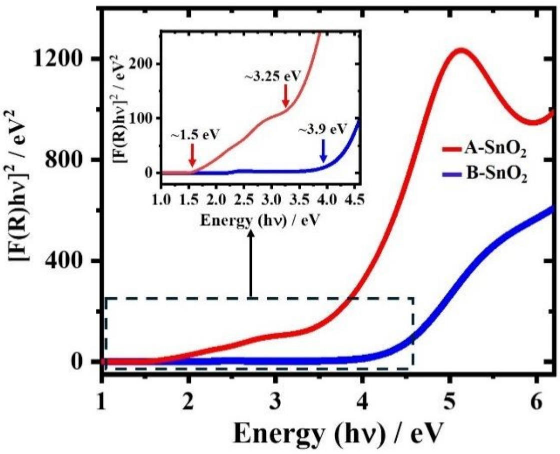

Fig. 7 UV-Vis spectroscopy in diffuse reflectance (DRS) mode for A-SnO_2 (red line) and B-SnO_2 (blue line) electrodes. Zoomed portion of the data is shown as inset, indicating the effective band-edges of A-SnO_2 and B-SnO_2.

Distinctive reduced effective absorption band-edge of the A-SnO_2 system (~3.25 eV and ~1.5 eV) in comparison to untreated B-SnO_2 (~4 eV) is evident in Fig. 7. The optical band edge of B-SnO_2 is consistent with the nanostructured SnO_2 systems. [58] However, UV-Vis plot of A-SnO_2 electrode with a lower band edge at 3.25 eV and below, indicate the incorporation of CuO nanostructures[59] into the SnO_2 system. The findings emphasize the interface induced effect in A-SnO_2 system, as a result of controlled growth and designed post deposition treatment of the thin-film SnO_2 on Cu current collector. The consistent results were obtained from attenuated total reflectance - Fourier transform infrared spectroscopy (ATR-FTIR), as demonstrated in the ESI†, Fig. S3†.

View Article Online
DOI: 10.1039/D5LF00261C

Results signify the controlled heat treatment induced interfacial phenomena at the SnO_2/Cu interface associated with the formation and dispersion/incorporation of CuO nanostructures into the SnO_2 nano-crystallites system. These results comply with the inference obtained from CV study, Fig. 4 in the earlier section.

Hence, the overall studies signify that the observed superior performance of post deposition heat treated SnO_2 electrode (A-SnO_2) in LIB relies on the formation of well-defined SnO_2 nano-crystallites along with the improved hierarchical surface morphology (see Fig. 6, the FESEM images) coupled with the interfacial phenomena. Such novel architecture of the electrode, results in significant enhancement in effective conductivity of the system, improved charge transfer properties, prevention of the pulverization, hindrance to Sn agglomeration and importantly contributing to an extra interfacial Li storage capacity to the system with the aid of Cu/Li_2O nanocomposites formation (as detailed in the earlier section).

Experimental

Preparation of binder-free SnO_2 based electrodes

To prepare the binder-free electrodes involving SnO_2 thin-film on Cu, RF-magnetron sputtering deposition technique was used to deposit SnO_2 on Cu sheets. The thin Cu sheet (9 µm thick, MTI Corporation) acts as current collector and substrate for SnO_2 sputter deposition. The SnO_2 target (two-inch diameter, 99.99% purity, Testbourne Ltd.UK) was used for sputtering purpose, at Ar gas (purity 99.999%) with a constant flow of 40 sccm, and sputtering power 50W. The distance between the target surface and the Cu foil was 14.1 cm. Base pressure and working pressure were maintained at ~2.5 x 10^{-5} bar and ~1.9 x 10^{-3} bar respectively. The substrate holder was rotating at 30 rpm and no heating has been applied on the substrate holder during the deposition process. The thickness of the SnO_2 was controlled by deposition time. The electrode mass was measured using electronic balance (Sartorius SECURA225D-10IN weighing balance with an accuracy of 0.01 mg) before and after SnO_2 loading on Cu current collector to calculate the mass of deposited SnO_2. In this method, first the total mass of the deposited SnO_2 electrode material on a piece of Cu foil or current collector (of size 7.8 cm X 2.8 cm) was measured, which was found to be 0.9 mg. From which active electrode mass was estimated as 0.07 mg, by considering the size or area of the circular electrode of diameter 15 mm, as used for the CR2032 coin-cell. The estimated mass of the deposited SnO_2 binder-free electrode was also cross verified thorough SnO_2 film thickness estimation via cross-sectional FESEM image, as displayed in the Fig. 1(b). The thickness of the deposited SnO_2 film was estimated from cross-sectional FESEM (Fig. 1(b)), as about 60 nm, considering the mass density of SnO_2 as 6.9 gm/cm^3, the electrode mass appears to be 0.07 mg (for 15 mm diameter electrode), which signify the consistency in the measurements and thus in the results.

View Article Online
DOI: 10.1039/D5LF00261C

After deposition, the SnO_2/Cu electrode was heat treated in a muffle furnace at a temperature of 400 ℃ for a short time period (about 10 minutes) in air atmosphere at ambient pressure. Before and after post deposition heat treated SnO_2 thin film (of about 60 nm thickness, with an active mass loading of 0.07 mg or with a mass density of 0.04 mg cm^{-2}) on Cu current collector systems were referred respectively as untreated SnO_2 electrode, "B-SnO_2" and electrode of interest, "A-SnO_2". Photographs of A-SnO_2, B-SnO_2 and bare Cu current collector are shown in the ESI†, Fig. S4†.

Assembling of coin cell and Electrochemical measurements

The electrochemical performances of the A-SnO_2 and B-SnO_2 working electrodes were investigated with CR2032 coin cells assembled in argon-filled glovebox (MBRAUN UNIlab Plus, Germany) in half-cell configuration with Li chip (diameter 15 mm) as the counter electrode. A tri-layer polypropylene-polyethylene-polypropylene (PP/PE/PP) membrane (Celgard 2325) was used as separator (diameter 20 mm). Electrolyte solution of 1M of $LiPF_6$ salt (Sigma Aldrich) was prepared with a mixture of dimethyl carbonate (DMC) and ethylene carbonate (EC) in a 1:1 volume ratio. The cyclic performance and galvanostatic charge/discharge (GCD) cycling tests were conducted using battery testing system (NEWARE BTS4000), and electrochemical workstations (CH instruments, CHI423B and CHI605E) at a current density of 0.3 A g^{-1}, over a voltage range of 0.02V to 1.8V, at room temperature. The specific charge and discharge capacities of the electrodes were determined by dividing the total electrode capacity by the electrode mass (mass of the SnO_2). Cyclic Voltammetry (CV) was conducted using electrochemical workstations (CHI605E) within a voltage range of 0.05 V to 1.8 V at a scan speed of 0.05 mV sec^{-1}. The electrochemical impedance spectroscopy (EIS) measurements were conducted using electrochemical workstation (CHI423B), applying a sine wave with an amplitude of 5.0 mV over the frequencies from 10^5 Hz to 0.05 Hz.

Characterization techniques

The morphological studies were conducted using field emission scanning electron microscope (FE-SEM Supra 55, Carl Zeiss, Germany). Cross-sectional FESEM images were taken using FEI Nova Nano SEM 450 Field Emission Scanning Electron Microscope. Optical characterization was carried out using Diffused reflectance spectroscopy (DRS) mode of UV-Visible spectrophotometer (Shimadzu UV-2600i) equipped with an integrating sphere, in the wavelength range of 200 nm to 1400 nm. The structural analysis of A-SnO_2 and B-SnO_2 samples were conducted using X-ray diffraction (XRD) technique using Rigaku SmartLab, Japan with Cu Kα X-ray source (40 kV, 1.2 kW). The XRD data were recorded at a scan speed of 0.1°/min at a 2θ range of 20-60° with a step size of 0.01°. The vibrational studies were conducted using ATR FTIR spectroscopy (L1600300 Spectrum TWO FTIR spectrometer, Perkin Elmer), at a wavenumber range of 900 cm^{-1} to 400 cm^{-1}. The X-ray photoelectron spectroscopy (XPS) measurement was recorded using SPECS Surface Nano Analysis GmbH, Germany, at a binding energy range of 1300 eV to 0 eV, using Al Kα (1486.1 eV) X-ray source (13kV, 100W). XPS study of pristine SnO_2 electrode (B-SnO_2) (as shown in Fig. 1(a)) was conducted using AIPES beamline (BL-02) of Indus-1 synchrotron source, RRCAT, Indore, India with an Omicron energy analyzer (EA-125, Germany). All the core level spectra were calibrated using C 1 s (284.6 eV) peak.

Conclusions

We demonstrate the interface induced significant stability, cycle-life, and overall high capacity of tin-oxide (SnO_2) based thin film electrode with Cu current collector in a rechargeable Li-ion battery (LIB). Post deposition, controlled heat treatment of optimized SnO_2 thin film on Cu current collector allows the augmented growth of structured interfaces, and overall hierarchical nanostructured morphology, which provide adequate electrical connectivity in the electrode system, making the system better conducting and more resilient towards the electrochemical cycling, suppressing the pulverization issues, exhibiting high stability and long cycle life. Moreover, the beneficial structured interface not only provides good electrical connectivity, but it also allows the growth of Cu/Li_2O nanocomposites from initial battery cycling process, which contributes to an extra Li storage and enhances the capacity effectively through interfacial charge storage mechanism via capacitive characteristic. Essentially the electrode yields a superior specific capacity deploying interfacial charge storage in addition.
Quantitatively, the prototype of rechargeable LIB consists of this light-weight, binder-free, cost-effective, environment friendly SnO_2 based electrode with Cu current collector, as demonstrated in this work (as A-SnO_2), and Li as counter electrode, delivers high reversible capacity, stability and remarkable cycle life (1430 mAh g^{-1} and about 1200 mAh g^{-1} after 100 and 500 cycles respectively at a current density 0.3 A g^{-1} (0.2C)), rate-performance (800 mAh g^{-1} at 3 A g^{-1} (2C) at 110 cycles), with high coulombic efficiency (98-99%), compared to conventional thin film anode based on SnO_2, with a low reversible capacity of about 700 mAh g^{-1} and 216 mAh g^{-1} at 100-cycle and 500-cycle at a same current density 0.3 A g^{-1} respectively (as demonstrated in this work for B-SnO_2, and other reported results in the literature based on SnO_2 thin film electrodes).
This electrode demonstrated a higher level of performance over the thin-film anodes used in equivalent micro battery systems reported in the literature (Table S1†). These findings highlight the potency of the SnO_2- based electrodes with interfacial engineering to suffice the needs for cost-effective light-weight microelectronic energy storage devices that can meet the industrial demands and paves the way to the design of advanced materials for next-generation energy storage systems in general.

Author contributions

Adi Pratap Singh and Banadeep Dutta: co-first authors, equal contribution, methodology, formal analysis, data curation, validation, investigation, visualization, writing-original draft. Sudeshna Chattopadhyay: corresponding author, conceptualization, funding acquisition, resources, methodology, project administration, writing-review & editing, visualization, validation, supervision.

Conflicts of interest

There are no conflicts to declare.

Data availability

The authors confirm that the data supporting the findings of this study are available within the article and in its ESI.†

Acknowledgements

We would acknowledge Indian Institute of Technology Indore for all kinds of support for this work. This work was supported by the Science and Engineering Research Board (SERB), India, Project No. CRG/2020/005595 for supporting this work. We would like to thank Dr. Uday Deshpande and Sachin Kumar (UGC- DAE CSR, Indore) for XPS measurements and Dr. Gunjan Verma (UGC-DAE CSR, Indore) for cross-sectional SEM measurements. We would also like to thank Dr. R. J. Choudhary and Mr. Sharad Karwal (UGC-DAE CSR, Indore) for XPS measurements at the Indus-1 synchrotron radiation source, RRCAT, Indore, India. A.P.S. is thankful to CSIR-UGC INDIA, New Delhi under the UGC-Ref. No. 221610040822, and B.D. is thankful to DST INSPIRE-INDIA, New Delhi under the Award No. IF210393 for providing the fellowships.

Footnote

†Electronic supplementary information (ESI) available. DOI:

Notes and References

1. G. De Carne, S. M. Maroufi, H. Beiranvand, V. De Angelis, S. D'Arco, V. Gevorgian, S. Waczowicz, B. Mather, M. Liserre and V. Hagenmeyer, *Electric Power Systems Research*, 2024, **236**, 110963.
2. F. Mwasilu, J. J. Justo, E.-K. Kim, T. D. Do and J.-W. Jung, *Renewable and Sustainable Energy Reviews*, 2014, **34**, 501-516.
3. S. Zhao, C. D. Sewell, R. Liu, S. Jia, Z. Wang, Y. He, K. Yuan, H. Jin, S. Wang, X. Liu and Z. Lin, *Advanced Energy Materials*, 2020, **10**, 1902657.
4. P. Poizot, S. Laruelle, S. Grugeon, L. Dupont and J. M. Tarascon, *Nature*, 2000, **407**, 496-499.
5. J. B. Goodenough and K.-S. Park, *Journal of the American Chemical Society*, 2013, **135**, 1167-1176.
6. H. B. Wu, J. S. Chen, H. H. Hng and X. Wen Lou, *Nanoscale*, 2012, **4**, 2526-2542.
7. (a) M. Armand and J. M. Tarascon, *Nature*, 2008, **451**, 652-657 ; (b) C.-X. Zu and H. Li, *Energy & Environmental Science*, 2011, **4**, 2614-2624.
8. (a) H. Wang, Y. Bai, S. Chen, X. Luo, C. Wu, F. Wu, J. Lu and K. Amine, *ACS Applied Materials & Interfaces*, 2015, **7**, 80-84 ; (b) D. Pal, A. Mathur, A. Singh, S. Pakhira, R. Singh and S. Chattopadhyay, *ChemistrySelect*, 2018, **3**, 12512-12523.
9. Y. Kang, C. Deng, Y. Chen, X. Liu, Z. Liang, T. Li, Q. Hu and Y. Zhao, *Nanoscale Research Letters*, 2020, **15**, 112.
10. K. Sun, T.-S. Wei, B. Y. Ahn, J. Y. Seo, S. J. Dillon and J. A. Lewis, *Adv Mater*, 2013, **25**, 4539-4543.
11. H. Liu, G. Zhang, X. Zheng, F. Chen and H. Duan, *International Journal of Extreme Manufacturing*, 2020, **2**, 042001.
12. L. Zhang, X. Liu, M. Zhong, Y. Zhou, Y. Wang, T. Yu, X. Xu, W. Shen, L. Yang, N. Liu, D. Wei and Z. Liu, *Applied Materials Today*, 2020, **20**, 100651.
13. P. G. de Gennes, *Reviews of Modern Physics*, 1985, **57**, 827-863.
14. (a) L. Bricotte, K. Chougrani, V. Alard, V. Ladmiral and S. Caillol, *International Journal of Adhesion and Adhesives*, 2024, **132**, 103673 ; (b) S. Kisin, P. G. T. van der Varst and G. de With, *Thin Solid Films*, 2007, **515**, 6853-6859.
15. E. M. Petrie, in *Joining Textiles*, eds. I. Jones and G. K. Stylios, Woodhead Publishing, 2013, pp. 225-274.
16. (a) L. I. Maissel, R. Glang and P. P. Budenstein, *Journal of The Electrochemical Society*, 1971, **118**, 114C ; (b) R. J. MacDonald and D. Haneman, *Journal of Applied Physics*, 1966, **37**, 3048-3056.
17. W.-J. Li, W.-Z. Shao, Q. Chen, L. Zhang, Y. Han, B.-A. Chen, Q. Wang and L. Zhen, *Physical Chemistry Chemical Physics*, 2018, **20**, 15618-15625.
18. M. N. Obrovac and V. L. Chevrier, *Chemical Reviews*, 2014, **114**, 11444-11502.
19. (a) J. Cabana, L. Monconduit, D. Larcher and M. R. Palacín, *Advanced Materials*, 2010, **22**, E170-E192 ; (b) T. Li, X. Li, Z. Wang, H. Guo and Y. Li, *Journal of Materials Chemistry A*, 2015, **3**, 11970-11975 ; (c) J. Leng, Z. Wang, X. Li, H. Guo, H. Li, K. Shih, G. Yan and J. Wang, *Journal of Materials Chemistry A*, 2017, **5**, 14996-15001 ; (d) T. Li, X. Li, Z. Wang, H. Guo, Y. Li and J. Wang, *Journal of Materials Chemistry A*, 2017, **5**, 13469-13474.
20. (a) J. Read, D. Foster, J. Wolfenstine and W. Behl, *Journal of Power Sources*, 2001, **96**, 277-281 ; (b) Y. Idota, T. Kubota, A. Matsufuji, Y. Maekawa and T. Miyasaka, *Science*, 1997, **276**, 1395-1397 ; (c) P. Meduri, C. Pendyala, V. Kumar, G. U. Sumanasekera and M. K. Sunkara, *Nano Letters*, 2009, **9**, 612-616 ; (d) Y. Wang, H. C. Zeng and J. Y. Lee, *Advanced Materials*, 2006, **18**, 645-649 ; (e) J. S. Chen and X. W. Lou, *Small*, 2013, **9**, 1877-1893.
21. (a) R. Retoux, T. Brousse and D. M. Schleich, *Journal of The Electrochemical Society*, 1999, **146**, 2472 ; (b) K. D. Kepler, J. T. Vaughey and M. M. Thackeray, *Journal of Power Sources*, 1999, **81-82**, 383-387.
22. R. Hu, D. Chen, G. Waller, Y. Ouyang, Y. Chen, B. Zhao, B. Rainwater, C. Yang, M. Zhu and M. Liu, *Energy & Environmental Science*, 2016, **9**, 595-603.
23. Y.-H. Jin, K.-M. Min, S.-D. Seo, H.-W. Shim and D.-W. Kim, *The Journal of Physical Chemistry C*, 2011, **115**, 22062-22067.
24. (a) B. Jiang, Y. He, B. Li, S. Zhao, S. Wang, Y.-B. He and Z. Lin, *Angewandte Chemie International Edition*, 2017, **56**, 1869-1872 ; (b) J. Ren, J. Yang, A. Abouimrane, D. Wang and K. Amine, *Journal of Power Sources*, 2011, **196**, 8701-8705 ; (c) S. D. Ponja, B. A. D. Williamson, S. Sathasivam, D. O. Scanlon, I. P. Parkin and C. J. Carmalt, *Journal of Materials Chemistry C*, 2018, **6**, 7257-7266.
25. R. Hu, H. Zhang, Z. Lu, J. Liu, M. Zeng, L. Yang, B. Yuan and M. Zhu, *Nano Energy*, 2018, **45**, 255-265.
26. R. Hu, G. H. Waller, Y. Wang, Y. Chen, C. Yang, W. Zhou, M. Zhu and M. Liu, *Nano Energy*, 2015, **18**, 232-244.

View Article Online
DOI: 10.1039/D5LF00261C

27. V. Aravindan, K. B. Jinesh, R. R. Prabhakar, V. S. Kale and S. Madhavi, *Nano Energy*, 2013, **2**, 720-725.
28. (a) L. Zu, Q. Su, F. Zhu, B. Chen, H. Lu, C. Peng, T. He, G. Du, P. He, K. Chen, S. Yang, J. Yang and H. Peng, *Advanced Materials*, 2017, **29**, 1701494 ; (b) J. Liang, X.-Y. Yu, H. Zhou, H. B. Wu, S. Ding and X. W. Lou, *Angewandte Chemie International Edition*, 2014, **53**, 12803-12807.
29. C. Xu, J. Sun and L. Gao, *Journal of Materials Chemistry*, 2012, **22**, 975-979.
30. A. A. AbdelHamid, A. Mendoza-Garcia and J. Y. Ying, *Nano Energy*, 2022, **93**, 106860.
31. (a) L. Yu, X. Zhou, L. Lu, X. Wu and F. Wang, *ChemSusChem*, 2020, **13**, 5361-5407 ; (b) E. Poorshakoor and M. Darab, *Journal of Energy Storage*, 2024, **75**, 109638.
32. B. Huang, J. Yang, Y. Zou, L. Ma and X. Zhou, *Electrochimica Acta*, 2014, **143**, 63-69.
33. (a) A. Sedky, N. Afify, A. Hakamy and A. M. Abd-Elnaiem, *Physica Scripta*, 2023, **98**, 125929 ; (b) A. Peter, P. Julio de and K. James, *Atkins' Physical Chemistry*, 2022; (c) E. O. G. A. A. O. Adesakin G. E and G. O. Okocha, *NIPES - Journal of Science and Technology Research*, 2023, **5**.
34. (a) M. Batzill, J. Kim, D. E. Beck and B. E. Koel, *Physical Review B*, 2004, **69**, 165403 ; (b) X. Liu, Y. Jiang, K. Li, F. Xu, P. Zhang and Y. Ding, *Materials Research Bulletin*, 2019, **109**, 41-48 ; (c) W. Li, C. Shen, G. Wu, Y. Ma, Z. Gao, X. Xia and G. Du, *The Journal of Physical Chemistry C*, 2011, **115**, 21258-21263 ; (d) F. A. Akgul, C. Gumus, A. O. Er, A. H. Farha, G. Akgul, Y. Ufuktepe and Z. Liu, *Journal of Alloys and Compounds*, 2013, **579**, 50-56.
35. A. R. Selvaraj, M. Hong, H. Koo, J. Mun and H.-K. Kim, *Journal of Power Sources*, 2024, **591**, 233821.
36. (a) T. Brousse, R. Retoux, U. Herterich and D. M. Schleich, *Journal of The Electrochemical Society*, 1998, **145**, 1 ; (b) J. P. Maranchi, A. F. Hepp and P. N. Kumta, *Electrochemical and Solid-State Letters*, 2003, **6**, A198 ; (c) R. Lin, S. Zhang, Z. Du, H. Fang, Y. Ren and X. Wu, *RSC Advances*, 2015, **5**, 87090-87097 ; (d) A. A. Arie and J. K. Lee, *Materials Science Forum*, 2013, **737**, 80-84 ; (e) Y. Xia, B. Sun, S. Zhu, S. Mao, X. Li, B. Guo, Y. Zeng, H. Wang and Y. Zhao, *Journal of Solid State Chemistry*, 2019, **269**, 132-137 ; (f) W. Chen, H. Zhang, B. Yang, B. Li and Z. Li, *Thin Solid Films*, 2019, **672**, 157-164 ; (g) F. Klein, R. Pinedo, P. Hering, A. Polity, J. Janek and P. Adelhelm, *The Journal of Physical Chemistry C*, 2016, **120**, 1400-1414 ; (h) L. Cao, D. Wang and R. Wang, *Materials Letters*, 2014, **132**, 357-360 ; (i) G. Evmenenko, T. T. Fister, D. B. Buchholz, Q. Li, K.-S. Chen, J. Wu, V. P. Dravid, M. C. Hersam, P. Fenter and M. J. Bedzyk, *ACS Applied Materials & Interfaces*, 2016, **8**, 19979-19986 ; (j) Y. Wang, Y.-F. Zhang, H.-R. Liu, S.-J. Yu and Q.-Z. Qin, *Electrochimica Acta*, 2003, **48**, 4253-4259 ; (k) N. Garino, A. Lamberti, R. Gazia, A. Chiodoni and C. Gerbaldi, *Journal of Alloys and Compounds*, 2014, **615**, S454-S458 ; (l) S. K. Sharma, M.-S. Kim, D. Y. Kim and J.-S. Yu, *Electrochimica Acta*, 2013, **87**, 872-879 ; (m) X. Teng, Y. Qin, X. Wang, H. Li, X. Shang, S. Fan, Q. Li, J. Xu, D. Cao and S. Li, *Nanoscale Research Letters*, 2018, **13**, 60.
37. (a) US20050164090, 2005 ; (b) US20110300447, 2001.
38. T. Brousse, D. Defives, L. Pasquereau, S. M. Lee, U. Herterich and D. M. Schleich, *Ionics*, 1997, **3**, 332-337.
39. (a) Y. Lei, N. Du, W. Liu, H. Wu and D. Yang, *Ionics*, 2019, **25**, 4651-4658 ; (b) L. Yang, T. Dai, Y. Wang, D. Xie, R. L. Narayan, J. Li and X. Ning, *Nano Energy*, 2016, **30**, 885-891.
40. H. Wang, Q. Liang, W. Wang, Y. An, J. Li and L. Guo, *Crystal Growth & Design*, 2011, **11**, 2942-2947.
41. Z. Chen, Y. Cao, J. Qian, X. Ai and H. Yang, *Journal of Materials Chemistry*, 2010, **20**, 7266-7271.
42. (a) C. Wang, A. John Appleby and F. E. Little, *Journal of Power Sources*, 2001, **93**, 174-185 ; (b) R. A. Guidotti and P. J. Masset, *Journal of Power Sources*, 2008, **183**, 388-398 ; (c) H. Mukaibo, T. Sumi, T. Yokoshima, T. Momma and T. Osaka, *Electrochemical and Solid-State Letters*, 2003, **6**, A218.
43. (a) L. E. Helseth, *Journal of Energy Storage*, 2021, **35**, 102304 ; (b) Y. Huang, M. Zhong, Y. Huang, M. Zhu, Z. Pei, Z. Wang, Q. Xue, X. Xie and C. Zhi, *Nature Communications*, 2015, **6**, 10310.
44. (a) A. Li, H. Song, W. Wan, J. Zhou and X. Chen, *Electrochimica Acta*, 2014, **132**, 42-48 ; (b) S. Q. Wang, J. Y. Zhang and C. H. Chen, *Scripta Materialia*, 2007, **57**, 337-340.
45. (a) Y. F. Zhukovskii, P. Balaya, E. A. Kotomin and J. Maier, *Physical Review Letters*, 2006, **96**, 058302 ; (b) J. Jamnik and J. Maier, *Physical Chemistry Chemical Physics*, 2003, **5**, 5215-5220.
46. (a) B. Zhao, F. Mattelaer, J. Kint, A. Werbrouck, L. Henderick, M. Minjauw, J. Dendooven and C. Detavernier, *Electrochimica Acta*, 2019, **320**, 134604 ; (b) A. Sahai, N. Goswami, S. D. Kaushik and S. Tripathi, *Applied Surface Science*, 2016, **390**, 974-983.
47. (a) W. Liu, P. Xiang, X. Dong, H. Yin, H. Yu, P. Cheng, S. Zhang and S. Shi, *Composites Part B: Engineering*, 2021, **216**, 108883 ; (b) J. Xie, X. Li, H. Lai, Z. Zhao, J. Li, W. Zhang, W. Xie, Y. Liu and W. Mai, *Angewandte Chemie International Edition*, 2019, **58**, 14740-14747 ; (c) Z. Li, G. Li, W. Xu, M. Zhou, C. Xu, M. Shi, F. Li, L. Chen and B. He, *ChemElectroChem*, 2018, **5**, 2774-2780.
48. (a) J. Li, E. Murphy, J. Winnick and P. A. Kohl, *Journal of Power Sources*, 2001, **102**, 294-301 ; (b) M. E. Orazem and B. Ulgut, *Journal of The Electrochemical Society*, 2024, **171**, 040526.
49. D. Guan, J. Li, X. Gao and C. Yuan, *Journal of Alloys and Compounds*, 2014, **617**, 464-471.
50. D. Cavaliere, A. Ikezawa, T. Okajima and H. Arai, *Journal of Power Sources*, 2024, **621**, 235316.
51. S. A. Palaparty, R. L. Patel and X. Liang, *RSC Advances*, 2016, **6**, 24340-24348.
52. L.-H. Wang, S. Gao, L.-L. Ren, E.-L. Zhou and Y.-F. Qin, *Frontiers in Chemistry*, 2021, **9**, 790659.
53. Y. Zhu, J. Li, M. S. Saleh, H. Pham, T. P. Plateau, R. Panat and J. Park, *Journal of Power Sources*, 2020, **476**, 228593.
54. (a) C. C. L. McCrory, S. Jung, I. M. Ferrer, S. M. Chatman, J. C. Peters and T. F. Jaramillo, *Journal of the American Chemical Society*, 2015, **137**, 4347-4357 ; (b) C. C. L. McCrory, S. Jung, J. C. Peters and T. F. Jaramillo, *Journal of the American Chemical Society*, 2013, **135**, 16977-16987 ; (c) B. Hirschorn, M. E. Orazem, B. Tribollet, V. Vivier, I. Frateur and M. Musiani, *Electrochimica Acta*, 2010, **55**, 6218-6227.
55. B. J. Wood and R. G. J. Strens, *Mineralogical Magazine*, 1979, **43**, 509-518.
56. S. Landi, I. R. Segundo, E. Freitas, M. Vasilevskiy, J. Carneiro and C. J. Tavares, *Solid State Communications*, 2022, **341**, 114573.

57. S. Aksoy, Y. Çağlar, M. Caglar and S. Ilican, *Journal of Nanoelectronics and Optoelectronics*, 2016, **11**, 115-121.

58. (a) M. Mezyen, G. El Fidha, N. Bitri, F. Harrathi, I. Ly and E. Llobet, *RSC Advances*, 2023, **13**, 31151-31166 ; (b) A. Ahmed, M. Naseem Siddique, U. Alam, T. Ali and P. Tripathi, *Applied Surface Science*, 2019, **463**, 976-985 ; (c) G. Pang, S. Chen, Y. Koltypin, A. Zaban, S. Feng and A. Gedanken, *Nano Letters*, 2001, **1**, 723-726.

59. (a) P. Vinothkumar, C. Manoharan, B. Shanmugapriya and M. Bououdina, *Journal of Materials Science: Materials in Electronics*, 2019, **30**, 6249-6262 ; (b) L. Xu, G. Zheng, S. Pei and J. Wang, *Optik*, 2018, **158**, 382-390 ; (c) Y. Wang, S. Lany, J. Ghanbaja, Y. Fagot-Revurat, Y. P. Chen, F. Soldera, D. Horwat, F. Mücklich and J. F. Pierson, *Physical Review B*, 2016, **94**, 245418 ; (d) N. Serin, T. Serin, Ş. Horzum and Y. Çelik, *Semiconductor Science and Technology*, 2005, **20**, 398.

View Article Online
DOI: 10.1039/D5LF00261C

Tin-oxide based binder-free light-weight nanostructured anode with high reversible capacity and cyclability for lithium-ion batteries manifesting the interfacial effect†

Adi Pratap Singh,†[a] Banadeep Dutta †[a] and Sudeshna Chattopadhyay *[a]

Data Availability Statement (DAS)

The authors confirm that the data supporting the findings of this study are available within the article and in its ESI.†